COMPLEX SPECTRAL-DOMAIN INDEPENDENT COMPONENT ANALYSIS OF ELECTROENCEPHALOGRAPHIC DATA

Jörn Anemüller, Terrence J. Sejnowski and Scott Makeig

Computational Neurobiology Laboratory
The Salk Institute for Biological Studies
La Jolla, California
{jorn,terry,scott}@salk.edu
and
Swartz Center for Computational Neuroscience
University of California San Diego
La Jolla, California

ABSTRACT

Independent component analysis (ICA) has proved to be a highly useful tool for modeling brain data and in particular electroencephalographic (EEG) data. In this paper, a new method is presented that may better capture the underlying source dynamics than ICA algorithms hereto employed for brain signal analysis. We suppose that a brief, impulse-like activation of an effective signal source elicits a short sequence of spatio-temporal activations in the measured signals. This leads to a model of convolutive signal superposition, in contrast to the instantaneous mixing model commonly assumed for independent component analysis of brain signals. In the spectral-domain, convolutive mixing is equivalent to multiplicative mixing of complex signal sources within distinct spectral bands. We decompose the recorded mixture of complex signals into independent components by a complex version of the infomax ICA algorithm. Some results from a visual spatial selective attention experiment illustrate the differences between real time-domain ICA and complex spectral-domain ICA, and highlight properties of the obtained complex independent components.

1. INTRODUCTION

The usefulness of independent component analysis (ICA) for the analysis of brain signals and in particular electroencephalographic (EEG) data has been demonstrated in several publications (e.g., [8, 10]), and ICA continues to be useful for building new models of experimental data. However, it is also well known that ICA algorithms presently applied to brain data rely on several idealized assumptions about the underlying processes which with some likelihood may not be fully applicable. While the results so far obtained with ICA speak for themselves and justify its continued use, it is nevertheless desirable to advance the ICA methodology by weakening its assumptions to allow more faithful modeling of EEG dynamics.

One principal limitation imposed on ICA algorithms is the assumed mixing process by which the source signals are superimposed to form the measured sensor signals. Presently, ICA analysis of brain data is carried out under the assumption of a linear and instantaneous mixing process which can be expressed mathematically as multiplication by a mixing matrix. The component signal sources are thought of as neural activity occurring in spatially fixed ensembles that each represent activity which is perfectly synchronized over the extent of each effective generator ensemble.

Perfectly synchronized activity might be too strong an assumption, not taking into account the spatio-temporal dynamics of the underlying neural processes. One way to allow the effective sources to exhibit more complex dynamics is to assume a convolutive mixing model. In a convolutive mixing process, a single EEG component may elicit a sequence of potential maps with varying spatial topography. Thereby, such a model may allow for, e.g., spatial propagation of EEG activity. Convolutive mixing in the time-domain is equivalent to multiplicative mixing in the frequency-domain with generally distinct complex-valued mixing coefficients in different frequency bands.

EEG researchers have long been familiar with the fact that EEG activity has distinctive characteristics in different frequency bands (conventionally delta, theta, alpha, beta, and gamma) which may be associated with different physiological processes. It may therefore be more appropriate to model the source superposition by a different mixing matrix for each frequency band.

Hence, we propose to approach independent component analysis of EEG signals through complex ICA applied to different spectral bands. The method consists of two processing stages (cf. Fig. 1). First, the measured EEG signals

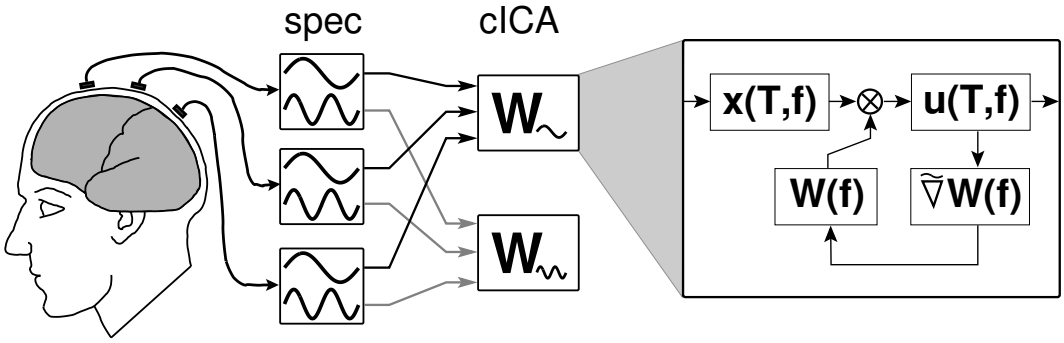

Fig. 1. Schematic representation of the processing stages of the complex spectral-domain ICA algorithm. Left ('spec'): the recorded electrode signals are decomposed into different spectral bands. Center ('cICA'): Complex ICA decomposition is performed within each spectral band. Right: Iteration steps performed by complex ICA for estimation of each separating matrix $\mathbf{W}(f)$.

are decomposed into different spectral bands, by short-time Fourier transformation or wavelet transformation, yielding a complex-valued spectro-temporal representation for each electrode signal. Then, a separate independent component analysis is performed on the complex frequency domain data within each spectral band, producing, for each band, a set of complex independent component activation time-courses and corresponding complex scalp maps. Furthermore, we investigate the case of a constrained complex ICA algorithm where the independent component (IC) activations remain complex, but the IC scalp maps are required to be real-valued.

The convolutive mixing model has previously been used for blind source separation in other domains, e.g., for speech signals. The physics of wave propagation in air directly leads to a convolutive mixing process (e.g., [2]). However, speech signals are generally modeled as wide-band sources, emitting energy essentially over the entire spectral range of interest. In contrast, this assumption cannot be made for brain signals, so that corresponding convolutive ICA algorithms cannot be applied directly to the problem at hand.

On the other hand, the case of narrow-band sources is encountered in applications for communications, leading to ICA algorithms which are similar to the one presented here [11]. However, one should bear in mind that the narrow-band assumption is also not completely justified for brain signal sources; an aspect, however, whose discussion would exceed the scope of the present paper.

The remainder of the paper is organized as follows: In sections 2.1 and 2.2, the employed spectral decomposition and the assumed mixing model are defined, respectively. A complex variant of the infomax ICA algorithm [5] is derived in section 2.3 from the maximum-likelihood principle, and a variant constrained to real scalp maps is discussed in section 2.3.1. Visualization of complex activations and maps is discussed in section 2.3.2. Results from a visual attention task EEG experiment are presented in section 3.

2. METHODS

2.1. Spectral decomposition

Consider measured signals $x_i(t)$, where $i = 1,\ldots,M$ denotes electrodes. Their spectral time-frequency representations are computed as

$$x_i(T,f) = \sum_{\tau} x_i(T+\tau) b_f(\tau), \tag{1}$$

where, f denotes center frequency, and $b_f(\tau)$ the basis function which extracts the spectral band f from the time-domain signal. The basis function is centered at time T. Hence, data of size [channels $i \times$ times t] is transformed into data of size [channels $i \times$ times $T \times$ frequencies f].

In this paper, we consider the decomposition by means of the short-time Fourier transformation, such that $b_f(\tau)$ is given by

$$b_f(\tau) = h(\tau)\, e^{-\mathrm{i}2\pi f\tau/2K}, \tag{2}$$

$h(\tau)$ being a windowing function (e.g., a hanning window) with finite support in the interval $\tau = -K,\ldots,K-1$, and $2K$ denoting the window length. Correspondingly, the frequency index acquires values $f = 0,\ldots,K$.

2.2. Mixing model

For each frequency band f the signals $\mathbf{x}(T,f) = [x_1(T,f), \ldots, x_M(T,f)]^T$ are assumed to be generated from independent sources $\mathbf{s}(T,f) = [s_1(T,f),\ldots,s_N(T,f)]^T$ by multiplication with a frequency specific mixing matrix $\mathbf{A}(f)$,

$$\mathbf{x}(T,f) = \mathbf{A}(f)\, \mathbf{s}(T,f), \tag{3}$$

with $\mathrm{rank}(\mathbf{A}(f)) = N$. Noise is assumed to be negligible. We restrict the presentation to square-mixing, $M = N$, but the methods are applicable to the case $M > N$.

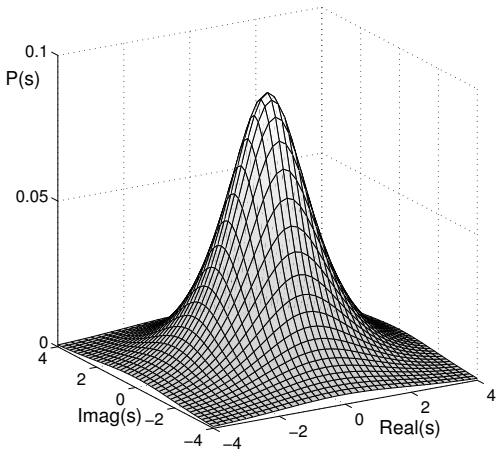

Fig. 2. Circular symmetric super-Gaussian probability density function $\mathcal{P}(s)$ of the complex sources s.

The estimates $\mathbf{u}(T,f)$ of the sources are obtained from the sensor signals by multiplication with frequency specific separating matrices $\mathbf{W}(f)$,

$$\mathbf{u}(T,f) = \mathbf{W}(f)\,\mathbf{x}(T,f). \tag{4}$$

2.3. Complex ICA

To derive a complex ICA algorithm, we model the sources $s_i(T,f)$ as complex random variables with a circular symmetric, super-Gaussian probability density function $\mathcal{P}_s(s)$. Since the phase $\arg(s_i(T,f))$ depends only on the relative position of the window centers T with respect to the time-domain signal $s_i(t)$, the property of circular symmetry of the distribution $\mathcal{P}_s(s)$ is a direct result of the window-centers being chosen independently of the signal. Hence, $\mathcal{P}_s(s)$ depends only on the magnitude $|s|$ of s and can be written as

$$\mathcal{P}_s(s) = g(|s|) \tag{5}$$

with the function $g(\cdot) : \mathbb{R} \to \mathbb{R}$ being a real-valued function of its real argument. The assumed two-dimensional distribution $\mathcal{P}_s(s)$ over the complex plane is illustrated in Fig. 2. The non-Gaussianity of the distribution is best seen by plotting the corresponding distribution $\mathcal{P}_{|s|}(|s|)$ for the *magnitude* $|s|$ versus the corresponding distribution (a Rayleigh distribution) derived from a two-dimensional Gaussian distribution of the same variance, as displayed in Fig. 3.

Using this source model together with the reconstruction model of Eq. (4) to obtain a maximum likelihood estimate [7] of the sources leads to the natural gradient [1] expression

$$\tilde{\nabla}\mathbf{W}(f) = \left(\mathbf{I} - \left\langle \mathbf{v}(T,f)\,\mathbf{u}(T,f)^H \right\rangle_T\right)\mathbf{W}(f), \tag{6}$$

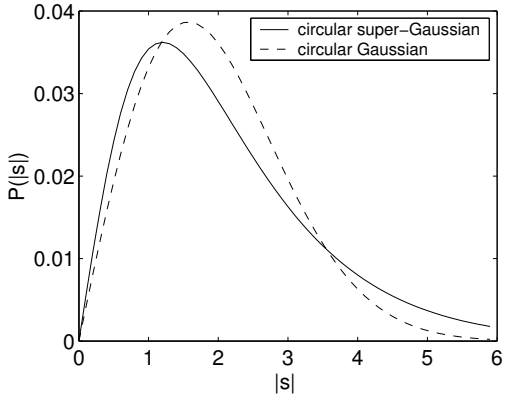

Fig. 3. The distribution $\mathcal{P}_{|s|}(|s|)$ of the sources' magnitude (solid) versus the distribution of the magnitude of a two-dimensional Gaussian of the same variance (dashed). The latter is the well-known Rayleigh distribution. The super-Gaussian source distribution is characterized by its strong peak at the origin and its long tails.

for the estimate of $\mathbf{W}(f)$, where

$$\mathbf{v}(T,f) = [v_1(T,f),\ldots,v_N(T,f)]^T, \tag{7}$$

$$v_i(T,f) = \operatorname{sign}(u_i(T,f))\,\frac{g'(|u_i(T,f)|)}{g(|u_i(T,f)|)}, \tag{8}$$

$$\operatorname{sign}(z) = \begin{cases} 0 & \text{if } z = 0, \\ z/|z| & \text{if } z \neq 0, \end{cases} \tag{9}$$

$\langle\cdot\rangle_T$ denotes expectation computed as the sample average over T, $g'(\cdot)$ is the first derivative of function $g(\cdot)$, and H denotes complex conjugation and transposition. The gradient Eq. (6) has previously been used as part of an algorithm for blind separation of speech signals [3].

For the choice

$$-\frac{g'(x)}{g(x)} = 1 - \frac{2}{1+e^{-x}} \tag{10}$$

we obtain a complex generalization of the standard infomax ICA learning rule [5]. In the case of purely real-valued data, the learning rule for complex data reduces to the infomax ICA learning rule for real signals.

The independent component decomposition based on Eq. (6) is performed separately for each frequency band f, yielding in total $N(K+1)$ complex independent component activation time-courses $u_i(T,f)$ and $N(K+1)$ complex scalp maps $\mathbf{a}_j(f)$, where $\mathbf{a}_j(f)$ denotes the j-th column of the estimated mixing matrix $\mathbf{A}(f) = \mathbf{W}^{-1}(f)$.

2.3.1. Complex ICA constrained to real scalp maps

The complex scalp maps $\mathbf{a}_j(f)$ can be interpreted in terms of amplitude- and phase-differences between different spatial positions elicited by the spatio-temporal dynamics of

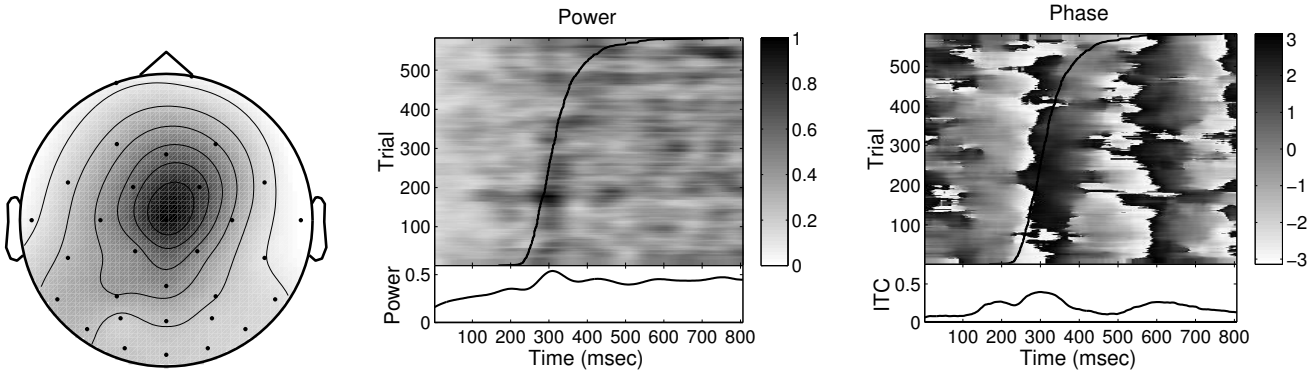

Fig. 4. Independent component (IC) at 5 Hz, obtained with separating matrix from standard time-domain infomax ICA. Left: Scalp map. Middle: Power ERP-image. Right: Complex-demodulated phase ERP-image. Response time superimposed on data. Lower panels: Event-related power (middle) and intertrial coherence (ITC, right).

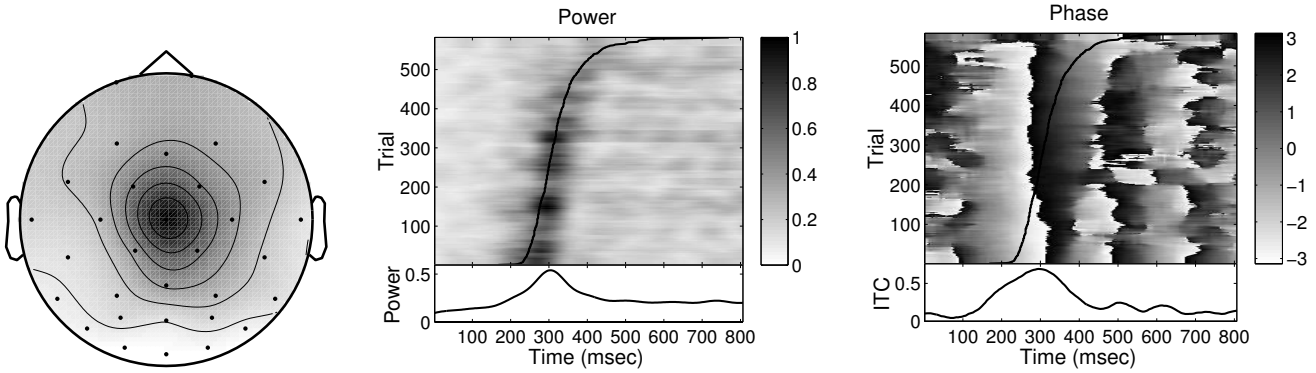

Fig. 5. IC at 5 Hz, obtained with real-map-constrained complex spectral-domain ICA, same dataset as Fig. 4. Left: Scalp map. Middle: Power ERP-image. Right: Complex-demodulated phase ERP-image. Response time and lower panels analogous to Fig. 4.

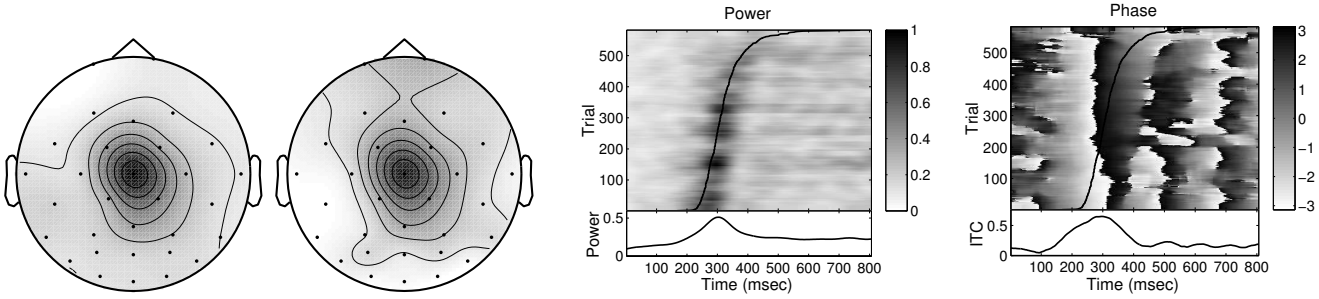

Fig. 6. IC at 5 Hz, obtained with fully complex spectral-domain ICA, same dataset as Figs. 4 and 5. From left to right: Magnitude and imaginary part of the complex scalp map, respectively; ERP-images of power and complex-demodulated phase of the complex IC activation time-courses, respectively. Response time and lower panels analogous to Fig. 4.

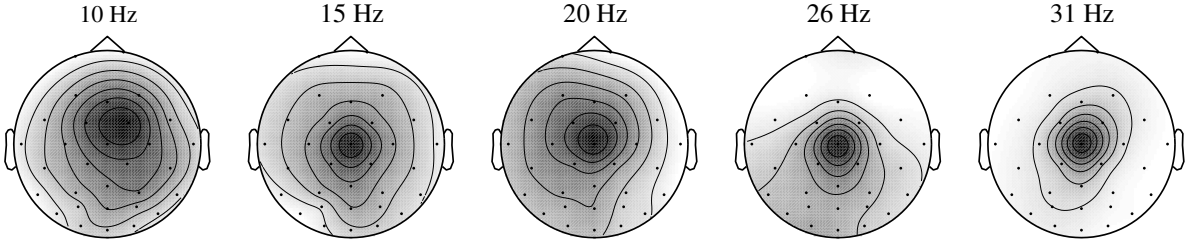

Fig. 7. Magnitude maps of complex independent components obtained using the fully complex spectral-domain ICA algorithm at five frequency bands, same dataset as Figs. 4-6.

EEG generators. It may, however, also be worthwhile to constrain the scalp maps to be real-valued, i.e., to correspond to amplitude differences only. Together with the simpler interpretation in terms of amplitude-differences, this approach has the advantage of making it possible to further separate the effects induced by wide-band versus band-limited data and by instantaneous (real) versus convolutive (complex) mixing. [1]

To constrain the algorithm's solution to real scalp maps, the initial estimate of $\mathbf{W}(f)$ is chosen to be real (typically the identity matrix), and the gradient Eq. (6) is projected to the real plane, resulting in the constrained gradient

$$\tilde{\nabla}_{\Re}\mathbf{W}(f) = \Re\left(\tilde{\nabla}\mathbf{W}(f)\right), \tag{11}$$

with $\Re$ denoting the real part.

While the corresponding scalp maps $\mathbf{a}_j(f)$ are real, the separated IC activations $\mathbf{u}(T,f)$ remain complex. Eq. (11) differs from, e.g., applying standard infomax ICA to the real-parts of $\mathbf{u}(T,f)$ in that its underlying source model Eq. (5) is still based on a distribution over the complex plane. As a result, the product $\mathbf{v}(T,f)\,\mathbf{u}(T,f)^H$ in Eq. (11) is evaluated using complex multiplication.

2.3.2. Visualizing complex IC activations and maps

Complex independent component activations $u_i(T,f)$ are best visualized by separately plotting their power (squared amplitude) and phase. In order to simplify the visual impression of the phase data, we compensate for the effect of phase-advancement due to the carrier frequency by performing complex demodulation on the IC activations, obtaining complex signals in the frequency band centered at 0 Hz, and plot the phase of the demodulated signals. For multi-trial data this results in two ERP-image plots [9, 6] (power, phase) per frequency f. Event-related power and intertrial coherence (ITC, [10]) are computed from multi-trial data by averaging across trials.

To visualize complex component maps, the invariance of the source model (5) with respect to rotation around the origin has to be taken into account. Therefore, for each complex map $\mathbf{a}_j(f) = [a_{1j}(f),\ldots,a_{Mj}(f)]^T$ any rotated version $c_j(f)\,\mathbf{a}_j(f)$ thereof constitutes an equivalent map, with $c_j(f)$ being an arbitrary unit-norm complex number. For visualization we plot real-part, imaginary-part, magnitude and phase of the map $\hat{\mathbf{a}}_j(f) = c_j(f)\,\mathbf{a}_j(f)$ for which the sum of the imaginary parts $\Im$ vanishes, i.e.,

$$\sum_i \Im\left(\hat{a}_{ij}(f)\right) = c_j(f)\sum_i \Im\left(a_{ij}(f)\right) = 0. \tag{12}$$

[1] Also signal superposition by means of different *real*-valued mixing matrices in distinct frequency bands corresponds to a convolutive mixing in the time-domain, namely, convolution with symmetric filters. However, this special case of convolutive mixing may be too restricted to fully accomplish the possible complexity of the underlying neuronal dynamics.

A map $\hat{\mathbf{a}}_j(f)$ with negligible imaginary part indicates that the corresponding EEG process may represent activity of a highly synchronized generator ensemble. A non-negligible imaginary part is equivalent to phase-differences between distinct scalp electrode positions which may be elicited by more complex spatio-temporal dynamics of the corresponding EEG process, e.g., spatial propagation of EEG activity.

3. RESULTS

In this section, we present some results obtained with the proposed algorithm. A more detailed investigation of the algorithm's properties, including verification of the underlying assumptions and comparison with time-domain ICA, is within the scope of a forthcoming publication [4].

Results are obtained from the analysis of a visual spatial selective attention experiment where the subject attended one out of five possible locations on a screen and was asked to respond by a button press as quickly as possible each time a target stimulus appeared in the attended location. For details on the experiment, see [9]. Included in the analysis are 582 trials from target stimulus epochs collected from a single subject. Each epoch is 1 s long, starting at $t = -100$ ms, and the data are aligned time-locked to stimulus presentation at $t = 0$ ms. For visual presentation, the trials are sorted in order of ascending response time and smoothed with a 30 trials wide rectangular window. Response time is plotted superimposed on the data. Event-related power and intertrial coherence (ITC) are plotted below the ERP-images for power and phase, respectively.

The data were recorded from 31 EEG electrodes at a sampling rate of 256 Hz and decomposed into 11 equidistantly spaced spectral bands with center frequencies from 0 Hz (DC) to 51.2 Hz in 5.12 Hz steps. Decomposition was performed by short-time Fourier transformation with a window length of 50 samples, a hanning window taper, and a window shift of 1 sample between successive analysis windows. This yielded 207 short-time spectra for each trial derived from analysis windows centered at times between 1.6 ms and 806.3 ms in 3.9 ms steps.

To decompose the data into independent components, the 582 trials were concatenated, resulting for each spectral band, $f = 0,\ldots,10$, and channel, $i = 1,\ldots,31$, in frames $T = 1,\ldots,120474$. Pre-training sphering of the data was not performed. The separating matrix $\mathbf{W}(f)$ was initialized with the identity matrix for all spectral bands.

The dataset was decomposed using both, the fully complex (Eq. 6) and the real-map-constrained (Eq. 11) algorithms. For comparison, the same dataset was also decomposed using real infomax ICA applied to the time-domain data $x_i(t)$; the obtained real separating matrix was then applied to the spectral-domain data $\mathbf{x}(T,f)$.

A large number of independent component maps and

activations were obtained for the different frequency bands. We focus on one set of components whose central-midline projections are similar to EEG features associated with orienting to novel stimuli.

These components' response to stimulus presentation is most marked in the 5-Hz band. Fig. 4–6 illustrate differences between the real infomax, real-map-constrained complex infomax and fully complex infomax ICs. The real infomax IC (Fig. 4) shows a clear increase in power near the median response time at about 300 ms, and a strong mean phase resetting which is visible near 300 ms as a phase-wrap (from $-\pi$ to π) and as a peak in the ITC.

The corresponding component obtained from real-map-constrained complex ICA at 5 Hz is displayed in Fig. 5. Its component map shares the spatial focus of maximum scalp projection with the time-domain IC map (cf. Fig. 4), but the spatial extent of the projection appears different. Comparing the complex activation time-courses, the real-map-constrained complex IC shows a stronger response-locked power increase near 300 ms which is also more closely linked to the response time (Fig. 5, center panel), and a more consistent phase-resetting (Fig. 5, right panel). This indicates, that spectral-domain ICA may reflect behavior and underlying brain processes more faithfully than time-domain ICA.

The magnitude map obtained by decomposing the 5-Hz band with the fully complex ICA algorithm (Fig. 6, left) appears similar to the real-constrained component map. The corresponding imaginary map (Fig. 6, second from left) has a non-negligible amplitude at the spatial focus of maximum scalp projection. This indicates that spatio-temporal dynamics may be present in the data which can be modeled with complex maps, but not with real maps. Here, the complex IC activations do not appear different from the activations obtained with the real-map-constrained complex algorithm. However, it can be shown (not presented here) that fully complex ICA results in IC activations with a higher degree of independence than those obtained with real-map-constrained complex ICA.

To illustrate the similarity of component maps over different spectral bands, Fig. 7 displays those maps from the 10-Hz to 31-Hz decompositions that best match the illustrated 5-Hz component. The maps in Fig. 7 were obtained using the fully complex ICA algorithm; only the magnitude maps are shown. While the location of maximum scalp projection remains similar, the maps exhibit differences in shape and spatial extent, further suggesting that the complex spectral-domain ICA algorithm may model aspects of the data which real ICA algorithms ignore.

4. CONCLUSION

We have presented a new method for the analysis of brain data and in particular electroencephalographic signals. The method is based on spectral decomposition of the sensor signals, and subsequent analysis within distinct spectral bands by means of a complex infomax algorithm for independent component analysis. We present experimental results indicating that complex spectral-domain independent components may model aspects of spatio-temporal dynamics in the data which real independent components ignore. Future work will focus on the relation between complex independent components and underlying brain processes.

Acknowledgments. We acknowledge support by the German Academic Exchange Foundation DAAD (J. A.) and by the Swartz Foundation.

5. REFERENCES

[1] S. Amari, A. Cichocki, and H. H. Yang. A new learning algorithm for blind signal separation. In D. Touretzky, M. Mozer, and M. Hasselmo, editors, *Advances in Neural Information Processing Systems 8*, pages 757–763, 1996.

[2] J. Anemüller. *Across-Frequency Processing in Convolutive Blind Source Separation*. PhD thesis, Dept. of Physics, University of Oldenburg, Oldenburg, Germany, 2001.

[3] J. Anemüller and B. Kollmeier. Adaptive separation of acoustic sources for anechoic conditions: A constrained frequency domain approach. *Speech Communication*, 39(1-2):79–95, Jan 2003.

[4] J. Anemüller, T. J. Sejnowski, and S. Makeig. Complex independent component analysis of frequency-domain electroencephalographic data. *(submitted)*, 2003.

[5] A. J. Bell and T. J. Sejnowski. An information maximization approach to blind separation and blind deconvolution. *Neural Computation*, 7:1129–1159, 1995.

[6] T.-P. Jung, S. Makeig, W. Westerfield, J. Townsend, E. Courchesne, and T. J. Sejnowski. Analysis and visulization of single-trial event-related potentials. *Human Brain Mapping*, 14(3):166–185, 2001.

[7] D. J. C. MacKay. Maximum likelihood and covariant algorithms for independent component analysis. Technical report, Dept.of Physics, Cambridge University, England, 1996.

[8] S. Makeig, A. Bell, T.-P. Jung, and T. J. Sejnowski. Independent component analysis of electroencephalographic data. In *Advances in Neural Information Processing Systems*, volume 8, pages 145–151, 1996.

[9] S. Makeig, M. Westerfield, T.-P. Jung, J. Covington, J. Townsend, T. J. Sejnowski, and E. Courchesne. Functionally independent components of the late positive event-related potential during visual spatial attention. *Journal of Neuroscience*, 19:2665–2680, 1999.

[10] S. Makeig, M. Westerfield, T.-P. Jung, S. Enghoff, J. Townsend, E. Courchesne, and T. J. Sejnowski. Dynamic brain sources of visual evoked responses. *Science*, 295:690–694, 2002.

[11] K. Torkkola. Blind signal separation in communications: Making use of known signal distributions. In *Proceedings of the 1998 IEEE Digital Signal Processing Workshop*, Bryce Canyon, UT, August 10-12 1998.